Applied Catalysis B: Environmental 334 (2023) 122794

Contents lists available at ScienceDirect

Applied Catalysis B: Environmental

journal homepage: www.elsevier.com/locate/apcatb

# Reactive nanostructured membrane with high permeate flux under an ultralow pressure for excellent removal of refractory organic matter in actual water

Wei Li [a,*], Kuanchang He [a], Longxiang Tang [a], Lingyu Chen [a], Xiaodong Xin [a], Gang Wang [b], Qian Liu [a], Jinxia Wang [a], Sihao Lv [a], Defeng Xing [c,*]

[a] Research Center for Eco-environmental Engineering, Dongguan University of Technology, Dongguan 523808, China
[b] School of Environment and Civil Engineering, Dongguan University of Technology, Dongguan 523808, China
[c] State Key Laboratory of Urban Water Resource and Environment, School of Environment, Harbin Institute of Technology, Harbin 150090, China

ARTICLE INFO

*Keywords:*
Reactive nanostructured membrane
Nanoconfinement effect
Peroxymonosulfate
Refractory organic matter
Co(IV)-oxo species

ABSTRACT

Herein, we report a novel reactive nanostructured membrane (RNM) which integrated functionalities of effective peroxymonosulfate activation and advection-enhanced mass transfer rates, synthesized by anchoring nano-$Co_3O_4$ inside the nanochannel of $Ti_3C_2$ MXene as a co-catalyst, which was simultaneously embedded into a nickel foam support (denoted as Co/$Ti_3C_2$ RNM). The outstanding properties were mainly attributed to electron migration regulation through the nanoconfinement effect and the d-band center of the Co/$Ti_3C_2$ heterostructure close to the energy of the Fermi level. A 75.5 – 85.8% 1,4-dioxane (1,4-D) degradation in actual groundwater and bio-treated landfill leachate was achieved under a low pressure using a peristaltic pump and a high permeate flux of 237.8 $L{\cdot}m^{-2}{\cdot}h^{-1}$, corresponding to an ultrafast residence time of 3.7 s, in a single-pass flow-through mode. Singlet oxygen and Co(IV)-oxo species were mainly responsible for the 1,4-D removal. This study provides a strategy for the synthesis method of RNM combining the advantages of high catalytic activity and permeate flux.

## 1. Introduction

Refractory organic matter (ROM), such as herbicides and endocrine disruptors, is a type of emerging micropollutants, which seriously threatens the health and safety of humans and the environment due to its prevalence and toxicity [1], showing resistance to natural degradation and biotreatment methods [2]. Therefore, employing effective treatment methods after biotreatment, such as advanced oxidation processes (AOPs), is imperative to remove ROM [3,4]. Recently, the radical and/or nonradical pathways for ROM treatment during peroxymonosulfate (PMS) activation have been widely investigated [5–8] which consider the fast reaction kinetics of radicals, the high selectivity of nonradicals for organics, and the low dependence of the treatment efficiency on the operating parameters (e.g., pH and background constituents) [9]. Transition metal ions (e.g., Co(II), Fe(II), Mn(II), and Cu(II)) are commonly used for catalytic PMS activation, and Co(II) is considered one of the most effective catalysts [10,11]. Most heterogeneous catalysts are nanoscale powders that exhibit high catalytic activity due to the exposure of more active sites and a short diffusion distance [12]. However, the required separation procedures combined with reduced catalyst reusability could increase operating costs. Moreover, the incomplete recovery of catalysts could lead to metal leaching into natural water bodies. Thus, sustainable, environmentally friendly, and highly efficient treatment methods need to develop for removing ROM.

Catalysts impregnated into suitable supports (e.g., metal foams, ceramics, and glass), applied as an electrode or a membrane, can be easily recovered and reused without the need for separation procedures [13–16]. However, long residence times in batch mode limit the practical application in natural water treatment. Porous membranes with water permeabilities driven by hydraulic pressure can address this demand using a single-pass flow-through mode [17]. Recently, porous reactive nanostructured membranes (RNMs) activated PMS (membrane/PMS system) is a promising AOP method, integrated fast catalytic oxidation and advection-enhanced mass transfer rates in a single membrane platform, and demonstrated the advantages of enhanced efficiency, easy operation, and short residence time, receiving increased attention for wastewater treatment [18–23]. Kim and co-workers reported that a two-dimensional (2D) graphene oxide membrane removed

* Corresponding authors.
*E-mail addresses:* liwei@dgut.edu.cn (W. Li), dxing@hit.edu.cn (D. Xing).

https://doi.org/10.1016/j.apcatb.2023.122794
Received 2 February 2023; Received in revised form 15 April 2023; Accepted 21 April 2023
Available online 23 April 2023
0926-3373/© 2023 Elsevier B.V. All rights reserved.

nearly 100% 1,4-dioxane (1,4-D) with a permeate flux of 2 $L \cdot m^{-2} \cdot h^{-1}$ (LMH) under a pressure of 2 bar, and the 1,4-D degradation kinetics was about 635 times higher in the flow-through process than that in the batch system [21]. However, with the premise of high ROM degradation performance, achieving a high and stable permeate flux for long-term operation remains a great challenge. A trade-off between permeability–degradation efficiency–energy cost (based on the applied pressure) as well as metal leaching performance should also be considered. Therefore, novel RNM techniques with extremely efficient ROM degradation performance, high permeate flux under low pressure, and strong stability are urgently needed for wastewater treatment.

Recently, nanoconfinement catalysis has received great attention due to enhanced adsorption capacity, reaction efficiency, and electron/mass transfer [24–27]. The nanoconfinement catalytic effect involves some intrinsic characteristics like electron/mass transfer, electronic state, and reaction energy, which could greatly change when catalysis is conducted in a confined space at the nanoscale. These effects improve the catalytic activity and then accelerate the reactions. For example, Meng et al. reported that membranes with nanoconfinement spaces synthesized from 2D materials consisting of Co-Cu oxide nanosheets achieved nearly 100% degradation of organic contaminants [24]. MXene, as a class of 2D material, exhibited extraordinary properties when it was well delaminated, including 2D characteristics similar to graphene, robust chemical and mechanical stability, excellent thermal conductivity, and favorable catalytic activity [28]. These results indicated that MXene is suitable as the substrate for nanoconfinement structures [26]. Moreover, MXene with numerous hydrophilic functionalities and a large specific surface area was demonstrated to spontaneously intercalate water from solution between its layers and thus formed nanoconfined fluids, providing a platform for nanoconfinement behaviors [25,29]. The presence of nanochannels in MXene to establish a controllable nanoscale interlayer space between adjacent catalyst nanosheets in the catalytic reaction is another essential factor to ensure the feasibility of nanoconfinement [26,30]. However, to the best of our knowledge, the mechanisms of nanoconfinement catalysis using MXene materials in the membrane/PMS system remain unclear. Our previous study reported a $Co_3O_4$@MXene plate as an efficient PMS activator to degrade 1,4-D with a rate constant of 2.41 $min^{-1}$ at PMS dosages of 4 mM [31]. Moreover, the as-increased oxygen vacancies greatly promoted the mobility of surrounding oxygen ions to generate reactive oxygen species (ROS), allowing the fast transformation of Co(II) and Co (III). Thus, we hypothesized that loading nano-$Co_3O_4$ impregnated into $Ti_3C_2$ MXene material on nickel foam support as an RNM and operated in the flow-through operation mode could promote the catalytic activity and ROM degradation efficiency in the membrane/PMS system. In addition, the effect of in situ generated high-valent metal-oxo species in the membrane/PMS system should be considered.

Herein, we report a novel RNM constructed by anchoring nano-$Co_3O_4$ inside $Ti_3C_2$ MXene as a co-catalyst ($Co/Ti_3C_2$) for nanoconfinement and loading the co-catalyst into the interlayer of double chip nickel foam (NF) for extremely low pressure-driven ROM removal in natural water, obtaining a high and stable permeate flux during long-term operation. Furthermore, the PMS adsorption/activation mechanism of the $Co/Ti_3C_2$ RNM/PMS system was elucidated by experiments and density functional theory (DFT) calculations for the first time. The degradation efficiency of the $Co/Ti_3C_2$ RNM/PMS system was investigated in actual groundwater and biotreated landfill leachate contaminated with 1,4-D, classified as toxic to humans and the environment [32]. The permeate flux and Co leaching performance during the long operation were also evaluated. In addition, we investigated the effluent PMS residue, a pollutant limiting the applicability of this approach, which has been ignored by most studies. Thus, this work provides a promising strategy to enhance the catalytic activities and permeability of RNM as well as insight into the mechanism of PMS adsorption/activation in the $Co/Ti_3C_2$ RNM/PMS system.

## 2. Materials and methods

### 2.1. Chemicals, materials, and actual water samples

Detailed information is provided in Text S1 and Tables S1 and S2 of the Supporting Information.

### 2.2. Fabrication of $Ti_3C_2$ MXene and $Co/Ti_3C_2$ reactive nanostructured membrane (RNM)

The synthesis of $Ti_3C_2$ MXene is described in Text S2. The overall fabrication process of $Co/Ti_3C_2$ RNM is illustrated in Fig. 1a. Briefly, tailored circular NF wafers (radius of 3 cm, thickness of 5 mm) were thoroughly cleaned with 0.5 M $H_2SO_4$, ethanol, and deionized water in sequence under ultrasonication for 15 min and dried for 3 h at 60 °C. Subsequently, 0.08 g nano-$Co_3O_4$ particles and 0.18 g $Ti_3C_2$ MXene were mixed in 40 mL anhydrous ethanol, and the mixture was dispersed by ultrasound (40 kHz in a sonicator bath) for 1 h to obtain a slurry. This slurry was dried in an oven (DZF-6050, AIHUA Instrument Equipment Co., Ltd., China) at 80 °C for 12 h to obtain a homogeneous mixture. This mixture was ground in a ball crusher (Pulverisette 6, Fritsch, Germany) at 1800 rpm for 20 min to obtain the precursor of $Co/Ti_3C_2$ co-catalyst (mixed $Co_3O_4$ + $Ti_3C_2$). Then, the preformed NF wafers were used to fabricate $Co/Ti_3C_2$ RNM using a spark plasma sintering (SPS) system (SPS-212HF, Fuji Electronic Industrial Co., Ltd., Japan). The sintering process was performed after the following steps: (1) 0.08 g of preformed $Co/Ti_3C_2$ catalyst in the middle of two pieces of NF wafers was placed in a graphite mold; (2) the system was evacuated to less than 1 Pa to ensure the exclusion of air; (3) the whole sintering process was operated under high temperature and high pressure for 40 min, and the following temperature profile was applied under vacuum: 0–5 min, room temperature to 400 °C; 5–15 min, 400–600 °C; 15–20 min, constant 600 °C; after 20 min, quick cooling to below 60 °C under vacuum [33]. The sintering pressure was kept at 4 MPa. In this process, the $Co/Ti_3C_2$ co-catalyst and RNM were simultaneously synthesized. Photographic images of fabricated $Co/Ti_3C_2$ RNM (radius of 3 cm, thickness of 1 mm) are shown in Fig. 1b.

### 2.3. Physicochemical characterization

The crystalline phase of the RNMs was identified by X-ray diffractometry (XRD, X′ Pert Pro MPD, Panalytical Co., Holland) using a Cu Kα radiation source. The morphology was investigated by scanning electron microscopy (SEM, Regulus 8100, HITACHI, Japan) and high-resolution transmission electron microscopy (HRTEM, FEI Tecnai G2 F30, Thermo Fisher Sci., USA). The elemental distribution was analyzed by energy-dispersive X-ray spectroscopy (EDX, Oxford X-Max 20, UK) coupled with SEM. The surface roughness was evaluated by atomic force microscopy (AFM, Bruker, Germany). X-ray photoelectron spectroscopy (XPS, ESCA Lab 250Xi, Thermo Fisher Sci., USA) was used to investigate the surface chemical composition and chemical bonds with a monochromatic Al Kα source. The porosity was determined with a mercury porosimeter (Micromeritic Autopore 9500, Norcross, GA). The hydrophobic property was evaluated by the contact angle of the water drop (DSA100s, Krüss Scientific Instruments Co., Ltd.).

### 2.4. Experimental degradation procedure of the peroxymonosulfate (PMS)/membrane system in flow-through mode

All flow-through mode experiments were carried out in a filtration reactor with a dead-end filtration apparatus using an effective membrane area of 28.3 $cm^2$ (Fig. S1 and Video S1) at different water fluxes, depending on the rotation speed of the peristaltic pump (Text S3). The water samples (groundwater and biotreated landfill leachate effluent spiked with a concentration close to the reported level in actual water bodies of 10 μM 1,4-D [34]) were driven using a peristaltic pump

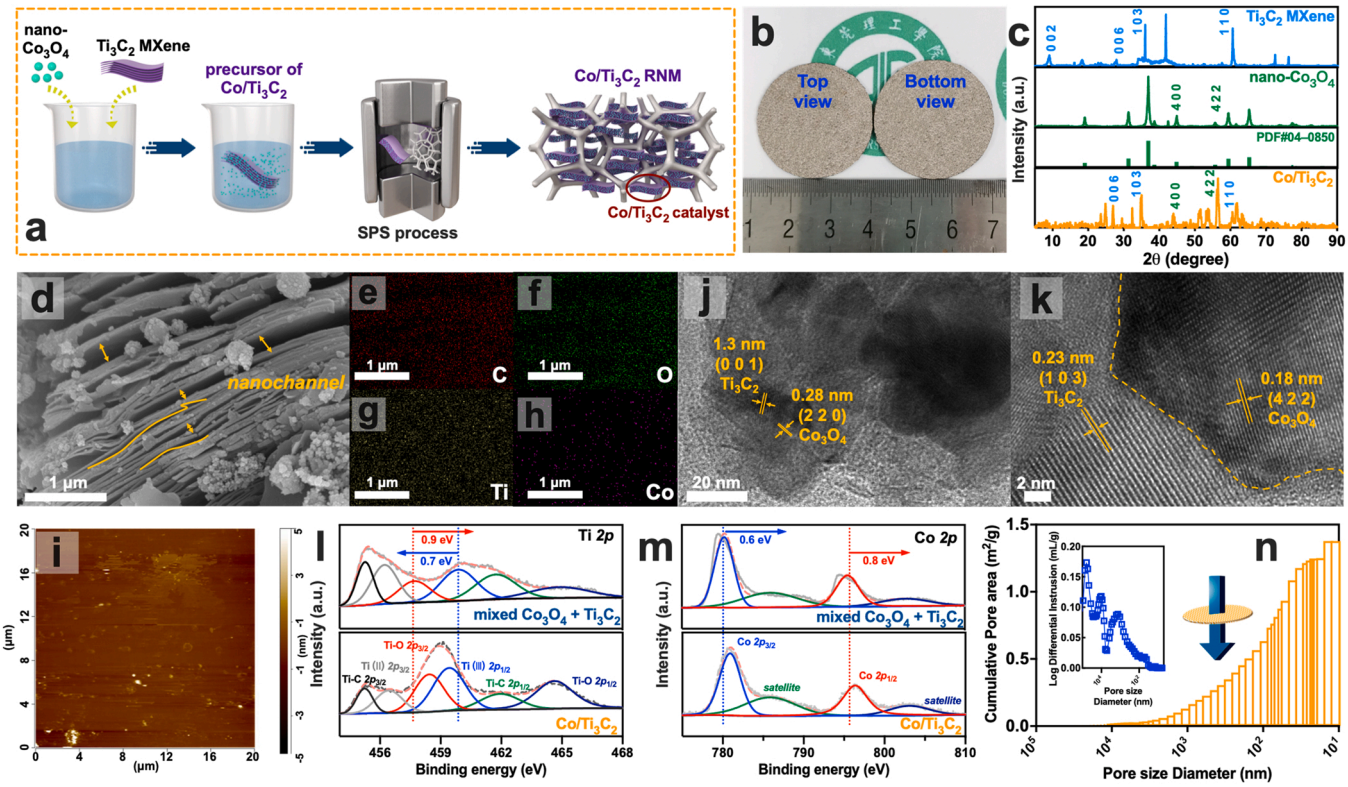


**Fig. 1.** (a) Schematic diagram of the fabrication process of the $Co/Ti_3C_2$ RNM (SPS: spark plasma sintering; RNM: reactive nanostructured membrane). (b) Photo of both sides of the $Co/Ti_3C_2$ RNM. (c) XRD patterns of $Ti_3C_2$ MXene, nano-$Co_3O_4$, and $Co/Ti_3C_2$. (d) SEM micrograph of $Co/Ti_3C_2$ co-catalyst; EDX images corresponding to (e) carbon, (f) oxygen, (g) titanium, and (h) cobalt. (i) AFM image and (j, k) HRTEM images of $Co/Ti_3C_2$ co-catalyst. (l, m) Deconvoluted spectra of Ti *2p* and O *1s* of $Co/Ti_3C_2$ co-catalyst inside the nickel foam support. (n) Mercury intrusion porosimetry to assess the pore size distribution of $Co/Ti_3C_2$ RNM.

(BT100–2 J, Longer Precision Pump Co., Ltd, Britain) with 2 r/min at 0.15 MPa. PMS was added in a concentration of 0.8 mM into the water sample feed before contacting the membranes. Samples (1 mL), after single-pass treatment within a time interval, were collected into a 2-mL tube containing 100 μL MeOH to quench the reaction and filtered through a 0.22-μm filter before analysis. In all experiments, the pH of the solution was not adjusted, and the experiments were performed at room temperature (25 ± 1 °C). The calculation of residence time and normalized decay rate constant (*k*) is described in detail in Text S4, and the results are listed in Table S3.

Supplementary material related to this article can be found online at doi:10.1016/j.apcatb.2023.122794.

### 2.5. Analytical methods

The concentrations of 1,4-D, sulfamethoxazole (SMX), bisphenol A (BPA), methyl phenyl sulfoxide (PMSO), methyl phenyl sulfone ($PMSO_2$), and furfuryl alcohol (FFA) (detailed description and results in Text S5 and Table S4) were determined by high-performance liquid chromatography (HPLC, Waters Co., USA) [35,36]. In order to eliminate the background interferences, the water samples were filtrated via 0.45 μM microfiltration membrane, and the filtrated blank samples were also detected. The residual PMS concentration was determined by iodometry (detailed description in Text S6) via a spectrophotometer (UV-3600, Shimadzu, Japan). Generated radicals and singlet oxygen ($^1O_2$) were indirectly identified by electron paramagnetic resonance (EPR) spectrometry (Bruker A200, Germany) using DMPO (0.2 M) and TEMP (0.2 M) as the spin-trapping agents, respectively [37]. The anion concentration was measured on an ion chromatography system (ICS-6000, Thermo Fisher Sci., USA) [38]. The leached cobalt concentration in samples was determined by inductively coupled plasma mass spectrometry (ICP-MS, ELEMENT XR, Thermo Fisher Sci., USA) [39]. The levels of total organic carbon (TOC) were tested using a TOC analyzer (Analytic Jena, Germany).

### 2.6. Density functional theory calculation (DFT)

Based on first principles, all DFT calculations of nano-$Co_3O_4/Ti_3C_2$ MXene were conducted via the Cambridge Serial Total Energy Package (CASTEP) module in Materials Studio [40]. After adjusting the lattice lengths and angles of the two materials, we cleaved the $Co_3O_4$ (4 2 2) plane based on XRD and SEM characterizations and extracted one layer of $Ti_3C_2$ to use as the substrate [41]. Then, a (2 ×1 ×1) supercell of $Co_3O_4$ and a (3 ×3 ×1) supercell of $Ti_3C_2$ were defined, and a vacuum thickness of 15 Å in the Z axis was constructed. The lattice lengths of the layered material were a = 14.951 Å, b = 11.258 Å, and c = 23.727 Å (Fig. S2). The bottom $Ti_3C_2$ layer was constrained while the atoms in $Co_3O_4$ were relaxed. The kinetic energy cutoff was set to 500 eV, and Brillouin zone integrations were sampled with Gamma point. Generalized gradient approximation (GGA) with Perdew-Burke-Ernzerhof (PBE) exchange-correlation functionals [42], and *Van Der Waals* dispersion corrections via the Tkatchenko-Scheffler method were applied [43]. A denser Monkhorst-Pack k-point grid of 1 × 3 × 1 was set in the density of states (DOS) calculations. The adsorption energy of PMS was further calculated as follows.

$$E_{ads} = E_{PMS-Co/Ti_3C_2} - E_{Co/Ti_3C_2} - E_{PMS} \quad (1)$$

where $E_{PMS-Co/Ti_3C_2}$, $E_{Co/Ti_3C_2}$, and $E_{PMS}$ represent the total energy of PMS adsorbate with $Co/Ti_3C_2$, layered model $Co/Ti_3C_2$, and free PMS molecule.

## 3. Results and discussion

### 3.1. Characterization and properties of the novel RNM

#### 3.1.1. Chemical composition and morphology

The chemical composition and morphology of the as-prepared Co/$Ti_3C_2$ RNM samples were thoroughly investigated. The XRD pattern of the Co/$Ti_3C_2$ co-catalyst layer indicated its successful synthesis by displaying characteristic facets of nano-$Co_3O_4$ and $Ti_3C_2$. Herein, the peaks at 44.0° and 56.5° were ascribed to the (4 0 0) and (4 2 2) planes of nano-$Co_3O_4$, while those at 27.0°, 35.0°, and 60.6° originated from the (0 0 6), (1 0 4), and (1 1 0) planes of $Ti_3C_2$ (Fig. 1c). The disappearance of the characteristic (0 0 2) $Ti_3C_2$ diffraction peak at 9.0° in Co/$Ti_3C_2$ implied the degradation of $Ti_3C_2$ and the decoration of the $Ti_3C_2$ surface with nano-$Co_3O_4$ at high temperature and pressure in the SPS process [44]. In addition, XRD results of the NF layer showed no obvious characteristic peaks except Ni, suggesting that the NF framework served as the support for water transport (Fig. S3). As depicted in Fig. 1d, the nano-$Co_3O_4$ is uniformly dispersed on the surface and inside $Ti_3C_2$ nanochannels with different nanoscales. Co/$Ti_3C_2$ RNM consisted of two NF layers and one Co/$Ti_3C_2$ co-catalyst layer according to the SEM image of the cross-section (Fig. S4). The presence and distribution of C, O, Ti, and Co elements in Co/$Ti_3C_2$ were visualized by elemental mapping (Fig. 1e−h and Fig. S5). Co/$Ti_3C_2$ was firmly deposited on the surface of the squashed three-dimensional (3D) porous Ni framework, corroborating the XRD results (Fig. S3).

The results of further AFM investigations revealed the highly homogeneous dispersal of Co/$Ti_3C_2$ on the NF framework (Fig. 1i and Fig. S6). HRTEM images also demonstrated the combination of nano-$Co_3O_4$ and $Ti_3C_2$ with lattice spacings of 0.18 and 0.20 nm, assigned to (4 2 2) and (4 0 0) facets of $Co_3O_4$, and 1.3 and 0.23 nm, assigned to the (0 0 1) and (1 0 3) facets of $Ti_3C_2$, respectively (Fig. 1j and k, and Fig. S7). Moreover, nano-$Co_3O_4$ attached to the edge of $Ti_3C_2$ (the orange dashed line) indicated the formation of a heterojunction from intimate contact of nano-$Co_3O_4$ and $Ti_3C_2$. The Co/$Ti_3C_2$ heterostructure was beneficial to generating numerous catalytically active sites, improving the Co(III)/Co(II) redox reaction rate, and accelerating the PMS activation [45,46].

To gain insights into the electronic structure changes of Co/$Ti_3C_2$ and its possible interactions across the heterostructure interface before and after the SPS fabrication process, the bonding mechanism of mixed nano-$Co_3O_4$ + $Ti_3C_2$ and as-synthesized Co/$Ti_3C_2$ were analyzed by XPS. Prominent shifts in peak position and shape were observed in the Ti XPS spectra (Fig. 1l). For both the mixture and Co/$Ti_3C_2$, the peaks assigned to Ti *2p* could be resolved into six components for Ti−C $2p_{3/2}$, Ti(II) $2p_{3/2}$, Ti−O $2p_{3/2}$, Ti(III) $2p_{1/2}$, Ti−C $2p_{1/2}$, and Ti−O $2p_{1/2}$. The peaks originating from Ti−O $2p_{3/2}$ at 457.5 eV positively shifted by 0.9 eV 458.4 eV, and Ti(III) $2p_{1/2}$ at 459.9 eV negatively shifted by 0.7 eV–459.2 eV [47]. Moreover, the intensities of Ti−C $2p_{3/2}$ and Ti−C $2p_{1/2}$ decreased, while those of Ti−O $2p_{3/2}$ and Ti−O $2p_{1/2}$ increased. These results showed that the SPS process could promote the transformations of Ti−C to Ti−O, which probably implied the formation of the chemical bond Ti−O−Co [13]. The Co $2p_{3/2}$ and Co $2p_{1/2}$ peaks of Co/$Ti_3C_2$ positively shifted by 0.6 eV 780.9 eV and 0.8 eV–796.3 eV compared to those of the mixture (780.3 and 795.5 eV, respectively) (Fig. 1m). In the Co spectrum, the great blueshifts in binding energy were ascribed to the decreased electron density around Co atoms [48], which possibly resulted from the strong electron redistribution induced by interfacial Ti−O−Co chemical bond formation [49]. The detailed XPS results of C and O *1s* are presented in Fig. S8 and Text S7. The higher binding energy of $O_{latt}$ in Co/$Ti_3C_2$ implied faster mobility of lattice oxygen species, contributing to the diffusion of lattice oxygen to oxygen vacancies [50]. The XPS analyses combined with the SEM and HRTEM characterizations demonstrated the successful fabrication of Co/$Ti_3C_2$ heterostructure with possible Ti−O−Co bond formation, which consequently led to improved electron transfer and enhanced PMS activation.

#### 3.1.2. Permeate flux

Mercury intrusion porosimetry results showed that the Co/$Ti_3C_2$ RNM had a median pore diameter of 1.69 μm with a porosity of 55.38%, and the cumulative pore area was about 1.4 $m^2/g$ (Fig. 1n). The pore size for water transport was larger than that of previous studies about PMS-activated membranes [19,21]. Moreover, the larger pore size could decrease the applied pressure and, thus, the energy consumption [8]. Abundant nanochannels of 6.03 − 90.26 nm created by layers of $Ti_3C_2$ sheets as scaffolds enabled specific catalytic functions under nano-confinement inside the Co/$Ti_3C_2$ co-catalyst [51–53]. In addition, membrane filtration could remove ROM by different molecular weight cutoffs and size exclusion [54], while the pore size available for water transport of Co/$Ti_3C_2$ RNM was far larger than that required for ROM. Thus, the distribution of molecular weight was negligible in this study. Using a pressure of 0.15 MPa in flow-through mode, the permeate fluxes of Co/$Ti_3C_2$ RNM were kept at 1206.0, 594.5, 322.7, 237.8, and 169.9 LMH with revolution speeds of the peristaltic pump of 1, 1.5, 2, 4, and 8 r/min, respectively. The water contact angle analyses showed that the Co/$Ti_3C_2$ RNM surface was extremely hydrophilic (Video S2), which was conducive for the diffusion of ROM and PMS in the microfluidic channels to the active surface sites.

Supplementary material related to this article can be found online at doi:10.1016/j.apcatb.2023.122794.

### 3.2. Efficiency of 1,4-D degradation under a high permeate flux

Because of its advantages (heterojunction interfaces with nano-confinement, high permeate flux, and increased oxygen vacancies), the Co/$Ti_3C_2$ RNM is a promising RNM for the membrane/PMS system. Thus, the ROM degradation performance of this membrane was further investigated (Fig. 2) by using different permeate fluxes and PMS dosages in the degradation of 1,4-D degradation (Fig. 2a-d). As expected, the addition of PMS exhibited negligible degradation of 1,4-D in the absence of the membrane (Fig. 2a). With decreasing permeate flux of Co/$Ti_3C_2$ RNM, the 1,4-D removal efficiency gradually increased, indicating the positive impact of long residence time. A 1,4-D removal of 85.8% was reached at a high permeate flux of 237.8 LMH, corresponding to a short residence time of only 3.7 s within the Co/$Ti_3C_2$ RNM. This residence time is much shorter than those of several minutes observed for various PMS-based AOPs [55,56]. Meanwhile, the TOC removal rate was 55.5% (Fig. S9). With a permeate flux of 1206.0 LMH corresponding to a shorter residence time of 0.8 s, the 1,4-D removal rate was 26.2%. As shown in Fig. 2b, the 1.4-D removal efficiency was not affected up to a residence time of 2.3 s. Above 2.3 s, a positive correlation ($R^2 = 0.99$) was established between rate constant and residence time, indicating that the trade-off between the 1,4-D removal efficiency and permeate flux was limited in the Co/$Ti_3C_2$ RNM/PMS system. Membrane filtration in the absence of PMS showed a very low 1,4-D removal rate of 5% (Fig. 2c). With increasing PMS dosage, the 1,4-D removal efficiency gradually increased. As shown in Fig. 2d, a positive correlation ($R^2 = 0.94$) was established between the rate constant and PMS dosage. The normalized volume $k_{app}$ of 1,4-D was found to be 27.8 times higher in the flow-through mode than in the batch mode (Fig. 2e and Fig. S10), which is consistent with the improvement of the mass transfer efficiency of PMS resulting in more efficient PMS activation and conversion to ROS [57,58]. The excellent 1,4-D removal was attributed to the efficient mass transfer realized in the flow-through process and the high oxidative degradation due to abundant active sites at the microfluidic channels of the Co/$Ti_3C_2$ RNM. The residual PMS concentration in the Co/$Ti_3C_2$ RNM/PMS system was mostly decomposed with increased residence time and decreased PMS dosages (Fig. 2f, g, details in Text S8). These results showed that PMS could be efficiently converted into other species (i.e., ROS) in the Co/$Ti_3C_2$ RNM/PMS system.

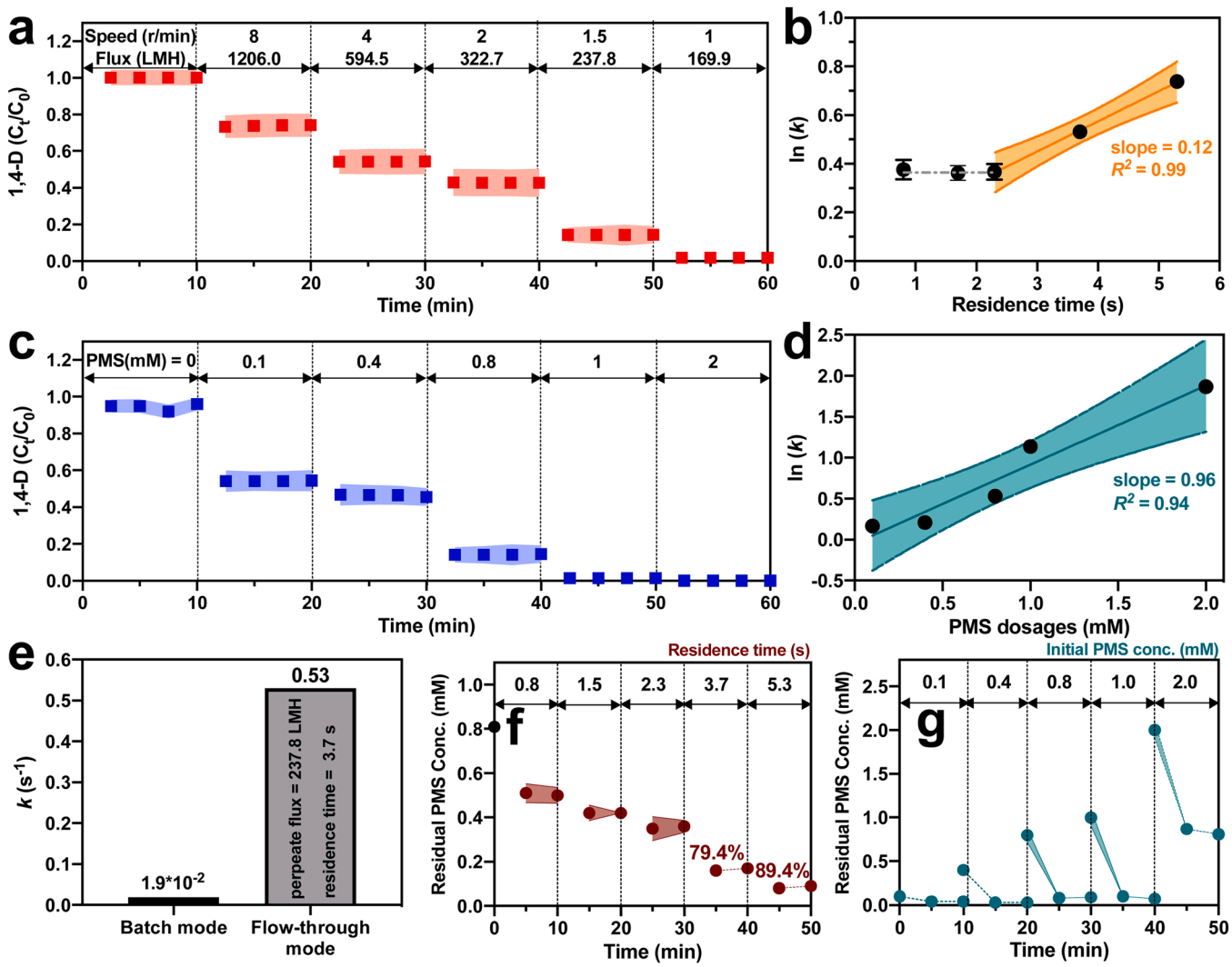


**Fig. 2.** Removal of 1,4-D from natural groundwater by the $Co/Ti_3C_2$ RNM/PMS system in flow-through mode (a) with different permeate fluxes (experimental conditions: $[1,4\text{-D}]_0$ = 10 μM, $[PMS]_0$ = 0.8 mM) and (c) with different PMS dosages (experimental conditions: $[1,4\text{-D}]_0$ = 10 μM, pump speed = 1.5 r/min, permeate flux = 237.8 LHM). Correlations between ln(*k*) and (b) retention time and (d) PMS dosages in the kinetic study according to (a) and (c). (e) Rate constant (*k*) of the $Co/Ti_3C_2$ RNM/PMS system in the batch and flow-through mode. Residual PMS concentration at 0, 5, and 10 min after 1,4-D removal in flow-through mode with different (f) retention times and (g) initial PMS dosages.

### 3.3. Degradation mechanism of the $Co/Ti_3C_2$ RNM

To identify the ROS generated in the $Co/Ti_3C_2$ RNM/PMS system, EPR tests were employed. Using DMPO as the trapping agent, the EPR spectra revealed the quadruple peak signals of DMPO-OH (1:2:2:1, $\alpha_N = \alpha_H$ = 14.9 G) and DMPO-$SO_4^{\bar{\cdot}}$ (1:1:1:1:1:1, $\alpha_N$ =13.7 G, $\alpha_H$ = 10.1 G) (Fig. 3a). The $^{\bullet}OH$ production was attributed to PMS activation according to the equation $HSO_5^- + e^- \rightarrow {}^{\bullet}OH + SO_4^{2-}$ [37]. When TEMP was used as the trapping agent, the triplet signal of TMPN (1:1:1, $\alpha_N = \alpha_H$ = 14.9 G) was detected (Fig. 3b), suggesting the presence of $^1O_2$ in the $Co/Ti_3C_2$ RNM/PMS system [59]. In addition, DMPOX and TEMPO at small intensity were observed when the pollutant was not in contact with the $Co/Ti_3C_2$ RNM, probably due to the self-decomposition of PMS [60]. Thus, $^{\bullet}OH$, $SO_4^{\bullet-}$, and $^1O_2$ were generated by the $Co/Ti_3C_2$ RNM/PMS system.

To elucidate the role of ROS in 1,4-D removal, quenching tests were performed in the $Co/Ti_3C_2$ RNM/PMS system using different ROS scavengers (Fig. 3c). It is well documented that methanol (MeOH), *tert*-butyl alcohol (TBA), L-histidine, catalase, *p*-benzoquinone (*p*-BQ), and PMSO are specific scavengers for $^{\bullet}OH$, both $^{\bullet}OH$ and $SO_4^{\bullet-}$, $^1O_2$, $H_2O_2$, $O_2^{\bullet-}$, and high valent metal-oxo species, respectively [61]. Results revealed that L-histidine inhibited 1,4-D removal by 83.4%, suggesting that $^1O_2$ was mainly responsible for 1,4-D removal (details shown in Text S9, Fig. S11). Quenching tests with catalase and *p*-BQ showed that 1,4-D degradation was inhibited by 39.4% and 33.8%, which was attributed to the fact that $H_2O_2$ and $O_2^{\bullet-}$ are the precursors of $^1O_2$ [8]. To confirm the amount of produced $^1O_2$, oxidation of FFA (as a probe of $^1O_2$, FFA is highly selective to $^1O_2$ with a rate constant of $1.2 \times 10^8$ $M^{-1}s^{-1}$) [59] was performed (Fig. 3d). No obvious FFA adsorption was observed in the absence of PMS (Fig. S12). In the presence of PMS, the results showed that the $Co/Ti_3C_2$ RNM converted 88% FFA within a single pass, also demonstrating that $^1O_2$ was mainly responsible for the nonradical pathway in the $Co/Ti_3C_2$ RNM/PMS system [62]. Moreover, $H_2O_2$ and $O_2^{\bullet-}/HO_2^{\bullet}$ were the dominating sources for $^1O_2$ generation as the nonradical mechanism in the $Co/Ti_3C_2$ RNM/PMS system (details shown in Text S10 and Fig. S13). A detailed discussion of the regulation of the catalyst active site and PMS adsorption/activation is provided in Section 3.5.

To investigate whether high-valent Co-oxo species were present in the $Co/Ti_3C_2$ RNM/PMS system, the specific probe PMSO was employed (Fig. 3e,f). The amounts of degraded PMSO and produced $PMSO_2$ in the $Co/Ti_3C_2$ RNM/PMS system were observed in both batch and flow-

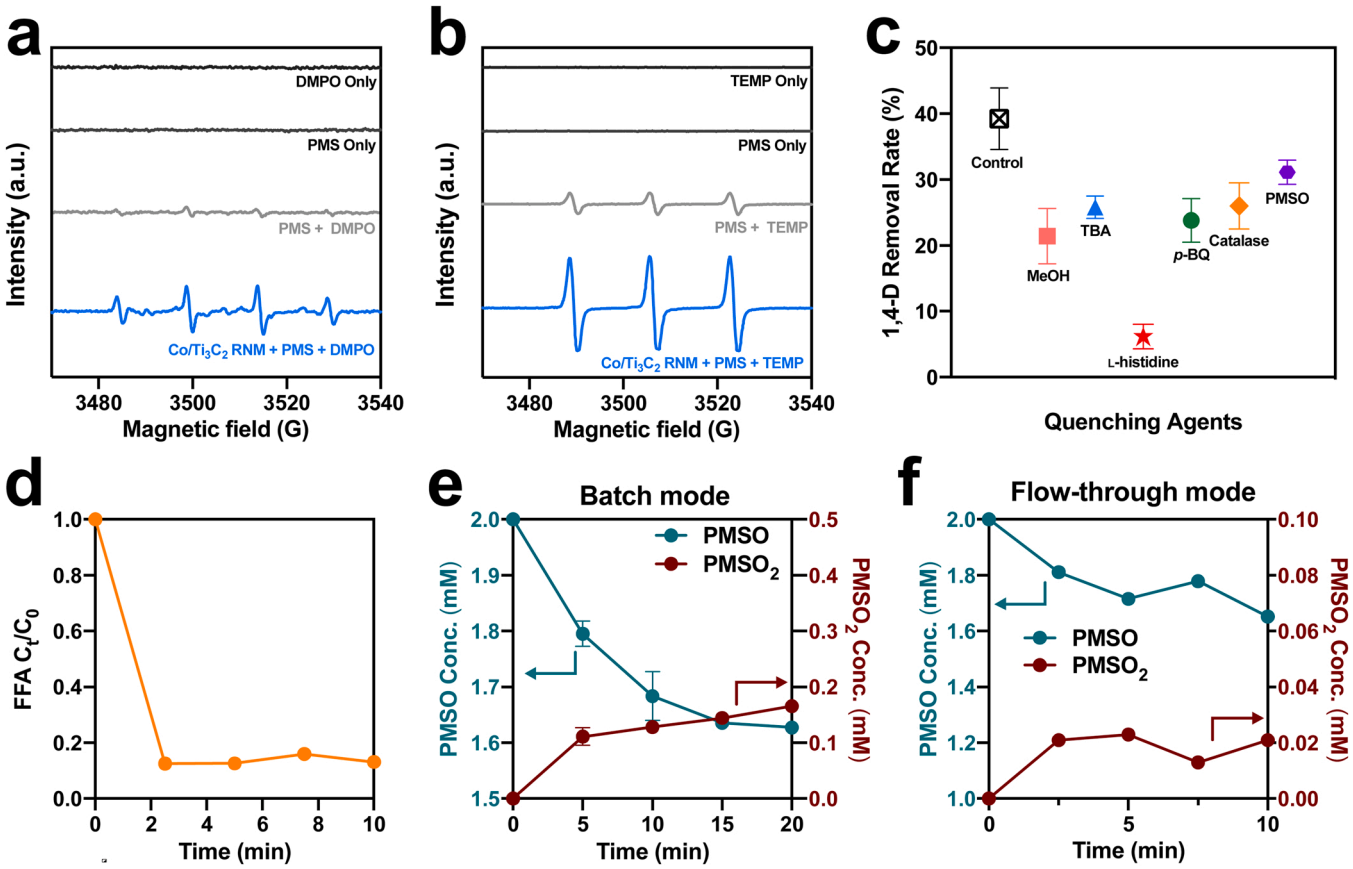


**Fig. 3.** EPR spectra of the Co/$Ti_3C_2$ RNM/PMS system using (a) DMPO and (b) TEMP as trapping agents. (c) ROS quenching tests by 0.5 M MeOH, TBA, L-histidine, *p*-BQ, catalase, and PMSO. (d) $^1O_2$ formation indicated by the degradation of FFA in the Co/$Ti_3C_2$ RNM/PMS system. PMSO loss and $PMSO_2$ generation in the Co/$Ti_3C_2$ RNM/PMS system in (e) batch and (f) flow-through mode. (Experimental conditions: $[1,4\text{-D}]_0$ = 10 μM, $[PMS]_0$ = 0.8 mM, pump speed = 1.5 r/min, permeate flux = 237.8 LHM, [DMPO] = [TEMP] = 0.2 M for (a) and (b), $[1,4\text{-D}]_0$ = 0.1 mM for (c), and $[FFA]_0$ = 0.5 mM for (d)).

through mode, which revealed that Co(IV)-oxo species were generated in the Co/$Ti_3C_2$ RNM/PMS system (details in Text S11). A recent study reported that Co-based catalysts activated PMS to produce Co(IV)-oxo species and exhibited superior performances for ROM removal within a wide pH range [63]. However, FFA and PMSO could both react with $^{\bullet}OH$ and $SO_4^{\bullet-}$ [64], resulting in a probable overestimation of the amounts of $^1O_2$ or Co(IV)-oxo species. In summary, the Co/$Ti_3C_2$ RNM/PMS system produced both free radicals and nonradicals for efficient ROM removal.

### 3.4. Stability and applicability of the Co/$Ti_3C_2$ RNM

To investigate the stability of Co/$Ti_3C_2$ RNM, consecutive flow-through operations of 168 h each were conducted. As shown in Fig. 4a, the 1,4-D removal rate with fresh and used Co/$Ti_3C_2$ RNM was similar (85.8 vs. 83.2%). The XPS results showed that the ratio of $O_{ads}$/$O_{latt}$ in the O *1s* spectra increased greatly from 0.67 to 1.86 as the $O_{latt}$ fraction decreased from 57.5% to 25.3% and the $O_{ads}$ fraction increased from 38.6% to 47.0% (details in Text S12, Fig. S14). In addition, Ti and

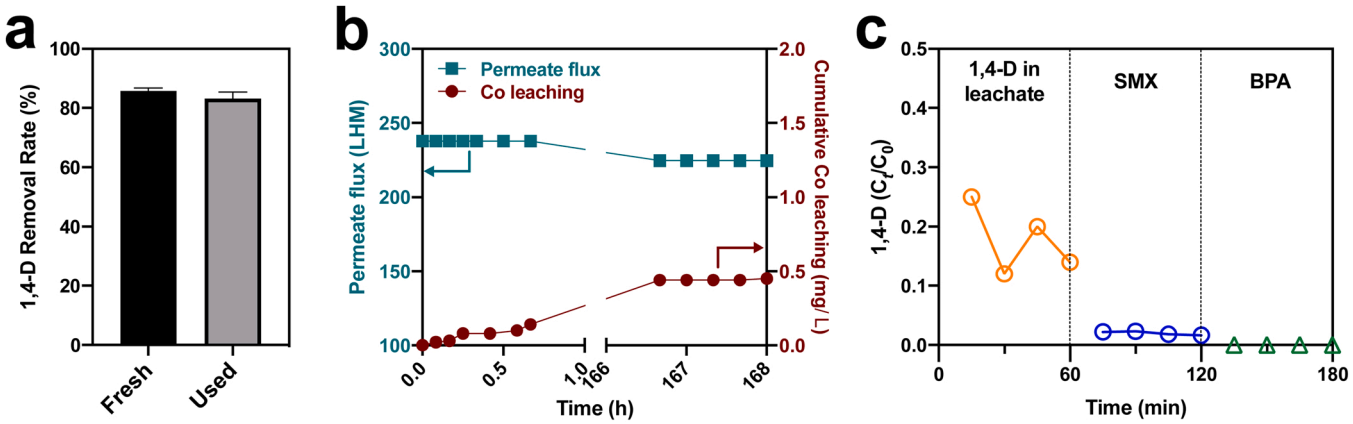


**Fig. 4.** (a) 1,4-D removal rate with fresh and used Co/$Ti_3C_2$ RNM. (b) Changes in the permeate flux and the cumulative Co leaching during flow-through operation for 168 h. (c) Application performance of 1,4-D removal in biotreated landfill leachate and SMX and BPA removal in groundwater. (experimental conditions: $[1,4\text{-D}]_0$ = $[SMX]_0$ = $[BPA]_0$ = 10 μM, $[PMS]_0$ = 0.8 mM, pump speed = 1.5 r/min, permeate flux = 237.8 LHM.).

Co chemical bonds exhibited small changes in fresh and used $Co/Ti_3C_2$ catalysts. The permeate flux of used $Co/Ti_3C_2$ RNM slightly decreased by 5.6% and was stable at 224.5 LMH after 168 h of operation (Fig. 4b), suggesting a negligible level of membrane fouling on the $Co/Ti_3C_2$ RNM. Co ions leaching in Co-based catalyst systems has been an issue of concern and subsequently affected their applicability [65]. The cumulative amount of leached Co increased slowly and was finally stable, corresponding to a concentration of 0.45 $mg{\cdot}L^{-1}$ after 168 h, which was below the Chinese standard of GB/T 25467–2010 for wastewater discharge. The advantageous low-level leaching was probably attributed to the strong chemical bond of Ti−O−Co after the SPS process. These results demonstrated that $Co/Ti_3C_2$ RNM could be considered a promising membrane for practical applications. To explore the wider applicability, the treatment of 1,4-D in biotreated landfill leachate, as well as of SMX and BPA in groundwater, was examined using the $Co/Ti_3C_2$ RNM/PMS system (Fig. 4c). The degradation of 1,4-D, SMX, and BPA amounted to 75.5–88.1%, 98.2%, and 100%, respectively, in single-pass mode. (Table 1).

### 3.5. Mechanistic insight into the PMS adsorption and activation of $Co/Ti_3C_2$

To explore the interfacial interaction of the $Co/Ti_3C_2$ heterostructure, DFT calculations were employed. Comparing Fig. S2a with b, obvious deformation of the geometric structure of $Co_3O_4$ with Ti−O−Co chemical bond formation occurred at the $Co/Ti_3C_2$ interface. This deformation may be ascribed to the relaxation generated during the geometry optimization of the continuous interface and the interaction between the $Co_3O_4$ and $Ti_3C_2$ [66]. The planar-averaged electron density difference could be used to describe the interaction. Note that electrons in $Co_3O_4$ were donated to $Ti_3C_2$, resulting in electron enrichment at the surface of $Ti_3C_2$ while the bottom of $Co_3O_4$ became electron-deficient (Fig. 5a and b) [67,68]. The theoretical calculations revealed efficient interfacial charge migration regulation, leading to the enhanced electron transmission from $Co_3O_4$ to $Ti_3C_2$, which was in good agreement with the XPS results (Fig. 1l and m, Fig. S8) [67]. Compared to $Ti_3C_2$, the higher electrostatic potential of $Co_3O_4$ in $Co/Ti_3C_2$ also demonstrated the movement of electrons from $Co_3O_4$ to $Ti_3C_2$ (Fig. 5c). This charge migration of $Co/Ti_3C_2$ would continue until the Fermi energy levels ($E_f$) achieve electronic equilibrium [67]. Moreover, the work function of $Co/Ti_3C_2$ was calculated as 4.495 eV. Furthermore, the electron run-off of $Co_3O_4$ may trigger Co(II) and Co(III) to transform into Co(IV). The enhanced electron transfer in $Co/Ti_3C_2$ could improve the catalytic performance, revealed by its electronic structure through the DOS spectrum (Fig. 5d). The active electron density with no gap near the Fermi energy level ($E_f = -0.425$ eV) suggested the metallic nature of $Co/Ti_3C_2$.

The projected density of states (PDOS) values of the elements revealed that d-band electrons from Co and Ti mainly contributed to the active electron density (Fig. S15), indicating that the majority of active

**Table 1**
Catalytic activity, permeate flux, and metal leaching of the membrane/PMS system in this work and previous studies.

| Membrane type | Organic contaminants | Organic contaminant concentration | PMS addition (mM) | Operation mode | Filtration mode | Reaction time | Removal rate (%) | Permeate flux ($L{\cdot}m^{-2}{\cdot}h^{-1}$) | Leaching | Ref. |
|---|---|---|---|---|---|---|---|---|---|---|
| $Pt/Al_2O_3$ membrane | BPA | 20 $mg{\cdot}L^{-1}$ | 2 | batch | – | 20 min | 100 | – | 0.37 $mg{\cdot}L^{-1}$ Al ion in 20 min | [15] |
| $Cu_1Co_1$ LDH@PAN membrane | SMX | 10 $mg{\cdot}L^{-1}$ | 0.24 | batch | – | 30 min | 95.2 | – | 0.023–0.093 $mg{\cdot}L^{-1}$ Co/Cu/Fe ion in 20 min | [16] |
| N-doped multi-walled CNT membrane | PE | 10 $mg{\cdot}L^{-1}$ | 5 | batch | – | 40 min | 100 | 136.5 | /[a] | [76] |
| $MnO_2$ ceramic membrane | HBA | 80 $mg{\cdot}L^{-1}$ | 6.5 | flow-through | circulation | 30 min | 98.9 | 193.5 | 12 $mg{\cdot}L^{-1}$ Mn ion in 6 h | [77] |
| CoAl-layered double hydroxide membrane | ranitidine | 2.5 $mg{\cdot}L^{-1}$ | 0.2 | flow-through | circulation | 20 min | 87.8<br>77.6 | 80<br>210 | 23 $\mu g{\cdot}L^{-1}$ Co ion in 1 h | [78] |
| FeCo@N-rGO CNT membrane | SMX | 10 $mg{\cdot}L^{-1}$ | 0.7 | flow-through | circulation | 30 min | 98.5 | 487.3 | 0.24–0.31 $mg{\cdot}L^{-1}$ Fe/Co ion in 30 min | [55] |
| $Co_3O_4$ @N-CNT membrane | SMX | 10 $mg{\cdot}L^{-1}$ | 0.7 | flow-through | circulation | 20 min | 98.9 | 125.5 | 0.016 $mg{\cdot}L^{-1}$ Co ion in 100 min | [56] |
| $Co_3O_4/C@SiO_2$ catalysis membrane | BPA | 1 $mg{\cdot}L^{-1}$ | 0.3 | flow-through | single pass | 3.1 s | 95 | 229 | 0.2 $mg{\cdot}L^{-1}$ Co ion | [19] |
| Co single atoms PVDF membrane | BPA | 2 μM | 10 | flow-through | single pass | 36 ms | > 90 | ~500 | < 0.1 $\mu g{\cdot}L^{-1}$ Co ion | [20] |
| Co single atoms graphene oxide membrane | 1,4-D | 50 $mg{\cdot}L^{-1}$ | 1 | flow-through | single pass | 0.9 s | 71.7 | 2.1 | 3% of the entire Co in 48 h | [21] |
| CuO ceramic hollow fiber membrane | BPA | 10 $mg{\cdot}L^{-1}$ | 0.5 | flow-through | single pass | –[b] | 98.2<br>83.4 | 40<br>200 | 0.12 $mg{\cdot}L^{-1}$ Cu ion in 30 min | [22] |
| Polyimide aerogel membrane | AO7 | 20 $mg{\cdot}L^{-1}$ | 1.3 | flow-through | single pass | –[b] | 96.2 | 50.8 | /[a] | [23] |
| $Co/Ti_3C_2$ RNM | 1,4-D | 10 μM | 0.8 | flow-through | single pass | 0.8 s<br>3.7 s | 26.2<br>85.8 | 1206.0<br>237.8 | 0.45 $mg{\cdot}L^{-1}$ Co ion in 168 h | This work |

*Note:* [a] No metal leaching, [b] Data not available.
*Abbreviations*: BPA, bisphenol A; 1,4-D, 1,4-dioxane; PE, phenol; HBA, 4-hydroxybenzoic acid; SMX, sulfamethoxazole; AO7, acid orange 7; N-rGO, nitrogen-doped reduced graphene oxide; N-CNT, nitrogen-doped carbon nanotube; LDH, layered double hydroxide; PAN, polyacrylonitrile; NF, nickel foam.

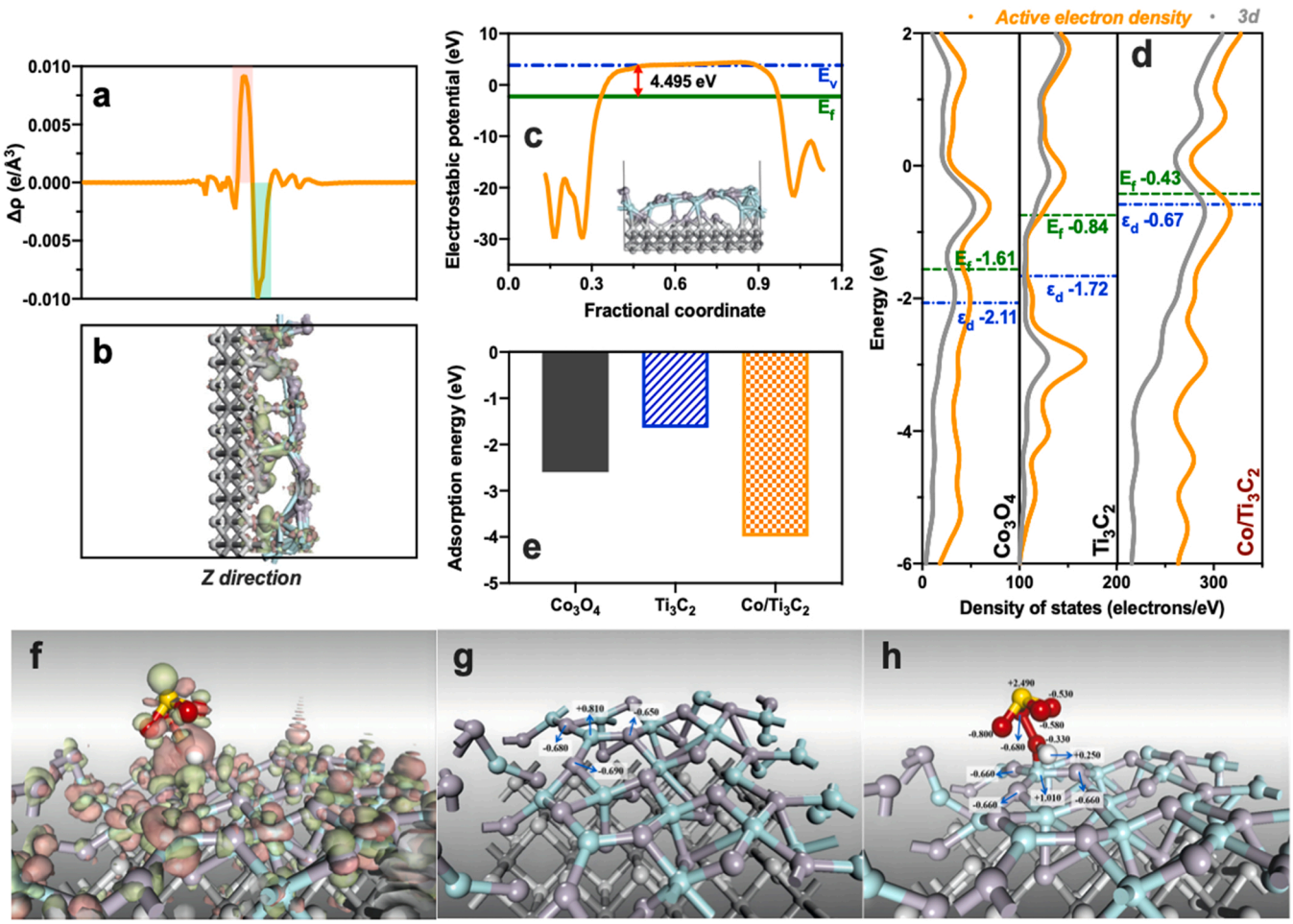


**Fig. 5.** DFT calculation studies of $Co/Ti_3C_2$, $Ti_3C_2$, and $Co_3O_4$ structures. (a) The line profile of planar-averaged electron density difference, the light green and pink blocks in the profile represent electron depletion and accumulation, respectively, and (b) the side view of the three-dimensional interfacial charge density difference. The calculated work functions and structural models of (c) $Co/Ti_3C_2$; the blue dashed line, and the dark green solid line denote the vacuum and Fermi energy levels. (d) DOS calculated for $Co_3O_4$, $Ti_3C_2$, and $Co/Ti_3C_2$. The dark green and blue dashed lines represent the Fermi energy level and the d-band center. (e) Adsorption energies of the PMS molecule on the surfaces of $Co_3O_4$, $Ti_3C_2$, and $Co/Ti_3C_2$. (f) The electron density difference results from the PMS adsorption on the surface of $Co/Ti_3C_2$. The charge number of the adsorption site and around the adsorption site (g) before PMS adsorption and (h) after PMS adsorption.

electrons were those d-electrons. To predict the intrinsic performance and electron transfer of $Co/Ti_3C_2$, we introduced a d-band center ($\varepsilon_d$) to further illustrate its catalytic ability. The parameter $\varepsilon_d$ is regarded as the descriptor for the d-band electrons, and fast intrinsic electron transfer and optimized catalytic properties can be anticipated when $\varepsilon_d$ is near $E_f$ [69,70]. As depicted in Fig. 5d, $\varepsilon_d$ of $Co/Ti_3C_2$ indicated an upward shift toward the vacuum level compared with $Co_3O_4$ and $Ti_3C_2$, which was 1.44 and 1.05 eV higher, resulting in the closest distance from $\varepsilon_d$ to $E_f$ for $Co/Ti_3C_2$. The quick charge mobility of $Co/Ti_3C_2$ and the high active electron state on the d band of Co could promote a faster redox cycle of Co(II)/Co(III), further contributing to the catalytic activity and stability of $Co/Ti_3C_2$ [71].

To exhibit the possible mechanism of PMS activation and ROS generation, DFT calculations on the interaction between the PMS molecule and the Co(II) reactive site were conducted. To the best of our knowledge, three pathways exist for PMS activation, including hydrogen O atom site (Metal-O(H)−O−$SO_3$), peroxy O atom site (Metal−O(OH)−$SO_3$), and terminal O atom site (Metal−$OSO_2$ −OOH) [72]. The detailed comparisons of the three models are shown in Text S13 and Fig. S16. The PMS adsorption energy ($E_{ads}$) of $Co/Ti_3C_2$ was calculated to be 3.99 eV, while those of $Co_3O_4$ and $Ti_3C_2$ were 2.60 and 1.64 eV (Fig. 5e). The $E_{ads}$ for PMS is directly related to the d-band electronic states of the transition metal catalyst ($Co/Ti_3C_2$) because the valence states of the PMS can couple with the d band of the $Co/Ti_3C_2$. This coupling can be described as the interaction between PMS and $Co/Ti_3C_2$, leading to the bonding and antibonding states [70,73]. Moreover, a closer distance from $\varepsilon_d$ to $E_f$ can produce empty antibonding states above $E_f$, resulting in larger $E_{ads}$ (Fig. 5d and e) [65]. The higher $E_{ads}$ demonstrated that $Co/Ti_3C_2$ had a higher affinity and chemical reactivity toward PMS than $Co_3O_4$ and $Ti_3C_2$. The enhanced PMS adsorption and activation were assigned to the effect of nanoconfinement within the nanochannels of $Co/Ti_3C_2$.

Fig. 5f displays the electron difference density (EDD) map of PMS in contact with $Co/Ti_3C_2$. The observed larger pink region presented a higher electron density surrounding the terminal O atom of PMS, which was the main activation site, indicating that the electrons of the Co atom were conducive to flowing toward the distal O atom in the peroxide bond (red) of PMS and trigger O−O bond cleavage for PMS activation. The Mulliken charge of the Co atom and the surrounding O atoms (light purple) also confirmed this result. The charge of the Co atom decreased by about 0.2e, while the charge transfer of the reactive sites in $Co_3O_4$ or $Ti_3C_2$ was weaker, 0.08e and 0.15e, respectively (Fig. 5g and h, Fig. S17). The decreased charge of the Co atom implied the shift to a higher valence state, promoting the transformation of Co(II) to Co(III) or even to Co(IV). Thus, the electron donations from the Co atom to PMS and the rate of the redox cycle between Co(II) and Co(III) were enhanced after the formation of the $Co/Ti_3C_2$ heterostructure, contributing to the O−O bond cleavage for PMS activation and the generation of ROS [74, 75].

## 4. Conclusions

In this study, we demonstrated the superior ROM removal performance of a novel RNM, synthesized through anchoring nano-$Co_3O_4$ inside the nanochannel of $Ti_3C_2$ MXene as a co-catalyst, which was simultaneously embedded into a nickel foam support. A 75.5 − 85.8% 1,4-D degradation in actual groundwater and bio-treated landfill leachate was achieved in a single-pass flow-through mode under low pressure, using a peristaltic pump and a high permeate flux of 237.8 LMH, corresponding to an ultrafast reaction time of 3.7 s. The SPS process could promote the transformations of Ti−C to Ti−O, which probably implied the formation of the chemical bond Ti−O−Co, which consequently led to improved electron transfer and enhanced PMS activation. The unique nanoconfinement effect through nano-$Co_3O_4$ anchored into the nanochannels of $Ti_3C_2$ improved the reaction kinetics and electron transfer, thereby enhancing catalytic activity. DFT calculations showed that the outstanding properties were mainly attributed to electron migration regulation through the nanoconfinement effect and the d-band center of the Co/$Ti_3C_2$ heterostructure being close to the energy of Fermi level. The quick charge mobility of Co/$Ti_3C_2$ and the high active electron state on the d band of Co could promote a faster redox cycle of Co(II)/Co(III), further contributing to the catalytic activity and stability. The strongly oxidizing generated singlet oxygen and Co(IV)-oxo species assisted rapid oxidative degradation and were mainly responsible for 1,4-D removal in the Co/$Ti_3C_2$ RNM/PMS system. This study provides a novel synthesis method of PMS-activation catalysts with nanoconfinement effects and of RNMs to promote the development of membrane/PMS systems. The selectivity of ROS formation inside and on the surface of Co/$Ti_3C_2$ RNM remained unclear and requires further studies.

## CRediT authorship contribution statement

**Wei Li**: Conceptualization, Investigation, Methodology, Formal analysis, Data curation, Funding acquisition, Writing – original draft, Writing – review & editing, Supervision. **Kuanchang He**: Methodology, Investigation, Data curation, Validation**. Longxiang Tang**: Data curation**. Lingyu Chen**: Data curation, Formal analysis**. Xiaodong Xin**: Resources, Investigation**. Gang Wang**: Methodology, Visualization**. Qian Liu**: Investigation, Data curation**. Jinxia Wang**: Formal analysis**. Sihao Lv**: Funding acquisition, Supervision. **Defeng Xing**: Supervision, Resources, Funding acquisition, Writing – review & editing.

## Declaration of Competing Interest

The authors declare that they have no known competing financial interests or personal relationships that could have appeared to influence the work reported in this paper.

## Data Availability

No data was used for the research described in the article.

## Acknowledgments

This study was supported by National Natural Science Foundation of China [U22A20443, 52000026], Guangdong Basic and Applied Basic Research Foundation [2022A1515140015], Characteristic Innovation Project of Guangdong Universities [2022KTSCX139], and Heilongjiang Key Research and Development Program [2022ZX02C19].

## Appendix A. Supporting information

Supplementary data associated with this article can be found in the online version at doi:10.1016/j.apcatb.2023.122794.

## References

[1] Y. Deng, C.M. Ezyske, Sulfate radical-advanced oxidation process (SR-AOP) for simultaneous removal of refractory organic contaminants and ammonia in landfill leachate, Water Res. 45 (2011) 6189–6194, https://doi.org/10.1016/j.watres.2011.09.015.

[2] P. Oulego, S. Collado, A. Laca, M. Diaz, Impact of leachate composition on the advanced oxidation treatment, Water Res. 88 (2016) 389–402, https://doi.org/10.1016/j.watres.2015.09.048.

[3] H. Wang, B. Liao, M. Hu, Y. Ai, L. Wen, S. Yang, Z. Ye, J. Qin, G. Liu, Heterogeneous activation of peroxymonosulfate by natural chalcopyrite for efficient remediation of groundwater polluted by aged landfill leachate, Appl. Catal. B Environ. 300 (2022), https://doi.org/10.1016/j.apcatb.2021.120744.

[4] L. Jin, S. You, Y. Yao, H. Chen, Y. Wang, Y. Liu, An electroactive single-atom copper anchored MXene nanohybrid filter for ultrafast water decontamination, J. Mater. Chem. A 9 (2021) 25964–25973, https://doi.org/10.1039/d1ta07396f.

[5] F. Jiang, B. Qiu, D. Sun, Advanced degradation of refractory pollutants in incineration leachate by UV/Peroxymonosulfate, Chem. Eng. J. 349 (2018) 338–346, https://doi.org/10.1016/j.cej.2018.05.062.

[6] G. Chen, G. Wu, N. Li, X. Lu, J. Zhao, M. He, B. Yan, H. Zhang, X. Duan, S. Wang, Landfill leachate treatment by persulphate related advanced oxidation technologies, J. Hazard. Mater. 418 (2021), 126355, https://doi.org/10.1016/j.jhazmat.2021.126355.

[7] J. Wang, S. Wang, Activation of persulfate (PS) and peroxymonosulfate (PMS) and application for the degradation of emerging contaminants, Chem. Eng. J. 334 (2018) 1502–1517, https://doi.org/10.1016/j.cej.2017.11.059.

[8] W. Li, R. Xiao, H. Lin, K. Yang, W. Li, K. He, L.H. Yang, M. Pu, M. Li, S. Lv, Electro-activation of peroxymonosulfate by a graphene oxide/iron oxide nanoparticle-doped $Ti_4O_7$ ceramic membrane: mechanism of singlet oxygen generation in the removal of 1,4-dioxane, J. Hazard. Mater. 424 (2021), 127342, https://doi.org/10.1016/j.jhazmat.2021.127342.

[9] J. Lee, U. von Gunten, J.H. Kim, Persulfate-based advanced oxidation: critical assessment of opportunities and roadblocks, Environ. Sci. Technol. 54 (2020) 3064–3081, https://doi.org/10.1021/acs.est.9b07082.

[10] P. Hu, M. Long, Cobalt-catalyzed sulfate radical-based advanced oxidation: A review on heterogeneous catalysts and applications, Appl. Catal. B: Environ. 181 (2016) 103–117, https://doi.org/10.1016/j.apcatb.2015.07.024.

[11] L. Peng, Y. Shang, B. Gao, X. Xu, $Co_3O_4$ anchored in N, S heteroatom co-doped porous carbons for degradation of organic contaminant: role of pyridinic N-Co binding and high tolerance of chloride, Appl. Catal. B Environ. 282 (2021), https://doi.org/10.1016/j.apcatb.2020.119484.

[12] M. Ahmad, A.L. Teel, R.J. Watts, Mechanism of persulfate activation by phenols, Environ. Sci. Technol. 47 (2013) 5864–5871, https://doi.org/10.1021/es400728c.

[13] J. Lim, Y. Yang, M.R. Hoffmann, Activation of peroxymonosulfate by oxygen vacancies-enriched cobalt-doped black $TiO_2$ nanotubes for the removal of organic pollutants, Environ. Sci. Technol. 53 (2019) 6972–6980, https://doi.org/10.1021/acs.est.9b01449.

[14] Y. Wang, H. Wang, J. Li, X. Zhao, Facile synthesis of metal free perylene imide-carbon nitride membranes for efficient photocatalytic degradation of organic pollutants in the presence of peroxymonosulfate, Appl. Catal. B Environ. 278 (2020), 118981, https://doi.org/10.1016/j.apcatb.2020.118981.

[15] Y. Wang, S. Hui, S. Zhan, R. Djellabi, J. Li, X. Zhao, Activation of peroxymonosulfate by novel Pt/$Al_2O_3$ membranes via a nonradical mechanism for efficient degradation of electron-rich aromatic pollutants, Chem. Eng. J. 381 (2020), 122563, https://doi.org/10.1016/j.cej.2019.122563.

[16] R. Guo, L.-c Nengzi, Y. Chen, Y. Li, X. Zhang, X. Cheng, Efficient degradation of sulfamethoxazole by CuCo LDH and LDH@fibers composite membrane activating peroxymonosulfate, Chem. Eng. J. 398 (2020), 125676, https://doi.org/10.1016/j.cej.2020.125676.

[17] J.R. Werber, C.O. Osuji, M. Elimelech, Materials for next-generation desalination and water purification membranes, Nat. Rev. Mater. 1 (2016) 16018, https://doi.org/10.1038/natrevmats.2016.18.

[18] S.R. Lewis, S. Datta, M. Gui, E.L. Coker, F.E. Huggins, S. Daunert, L. Bachas, D. Bhattacharyya, Reactive nanostructured membranes for water purification, Proc. Natl. Acad. Sci. USA 108 (2011) 8577–8582, https://doi.org/10.1073/pnas.1101144108.

[19] J. Xie, Z. Liao, M. Zhang, L. Ni, J. Qi, C. Wang, X. Sun, L. Wang, S. Wang, J. Li, Sequential ultrafiltration-catalysis membrane for excellent removal of multiple pollutants in water, Environ. Sci. Technol. 55 (2021) 2652–2661, https://doi.org/10.1021/acs.est.0c07418.

[20] C. Chu, J. Yang, X. Zhou, D. Huang, H. Qi, S. Weon, J. Li, M. Elimelech, A. Wang, J. H. Kim, Cobalt single atoms on tetrapyridomacrocyclic support for efficient peroxymonosulfate activation, Environ. Sci. Technol. 55 (2021) 1242–1250, https://doi.org/10.1021/acs.est.0c06086.

[21] X. Wu, K. Rigby, D. Huang, T. Hedtke, X. Wang, M.W. Chung, S. Weon, E. Stavitski, J.H. Kim, Single-atom cobalt incorporated in a 2D graphene oxide membrane for catalytic pollutant degradation, Environ. Sci. Technol. 56 (2022) 1341–1351, https://doi.org/10.1021/acs.est.1c06371.

[22] S. Wang, J. Tian, Q. Wang, F. Xiao, S. Gao, W. Shi, F. Cui, Development of CuO coated ceramic hollow fiber membrane for peroxymonosulfate activation: a highly efficient singlet oxygen-dominated oxidation process for bisphenol a degradation, Appl. Catal. B Environ. 256 (2019), 117783, https://doi.org/10.1016/j.apcatb.2019.117783.

[23] X. Zhao, X. Yi, J. Song, X. Yuan, S. Yu, Y. Nie, J. Zhang, G. Cao, Mesoporous and flexible polyimide aerogel as highly active catalytic membrane for AO7

degradation by peroxymonosulfate activation, Chem. Eng. J. 431 (2022), 134286, https://doi.org/10.1016/j.cej.2021.134286.
[24] C. Meng, Z. Wang, W. Zhang, L. Cui, B. Yang, H. Xie, Z. Zhang, Laminar membranes assembled by ultrathin cobalt-copper oxide nanosheets for nanoconfined catalytic degradation of contaminants, Chem. Eng. J. 449 (2022), https://doi.org/10.1016/j.cej.2022.137811.
[25] L. Ding, L. Li, Y. Liu, Y. Wu, Z. Lu, J. Deng, Y. Wei, J. Caro, H. Wang, Effective ion sieving with $Ti_3C_2T_x$ MXene membranes for production of drinking water from seawater, Nat. Sustain. 3 (2020) 296–302, https://doi.org/10.1038/s41893-020-0474-0.
[26] W. Zhu, L. Ren, C. Lu, H. Xu, F. Sun, Z. Ma, J. Zou, Nanoconfined and in situ catalyzed $MgH_2$ self-assembled on 3D $Ti_3C_2$ MXene folded nanosheets with enhanced hydrogen sorption performances, ACS Nano (2021), https://doi.org/10.1021/acsnano.1c08343.
[27] S. Zhang, T. Hedtke, X. Zhou, M. Elimelech, J.-H. Kim, Environmental applications of engineered materials with nanoconfinement, ACS EST Eng. 1 (2021) 706–724, https://doi.org/10.1021/acsestengg.1c00007.
[28] S. Wang, Z. Li, G. Wang, Y. Wang, Z. Ling, C. Li, Freestanding $Ti_3C_2T_x$ MXene/prussian blue analogues films with superior ion uptake for efficient capacitive deionization by a dual pseudocapacitance effect, ACS Nano 16 (2022) 1239–1249, https://doi.org/10.1021/acsnano.1c09036.
[29] V. Augustyn, Y. Gogotsi, 2D materials with nanoconfined fluids for electrochemical energy storage, Joule 1 (2017) 443–452, https://doi.org/10.1016/j.joule.2017.09.008.
[30] X. Tong, S. Liu, Y. Zhao, L. Huang, J. Crittenden, Y. Chen, MXene composite membranes with enhanced ion transport and regulated ion selectivity, Environ. Sci. Technol. 56 (2022) 8964–8974, https://doi.org/10.1021/acs.est.2c01765.
[31] W. Li, W. Li, K. He, L. Tang, Q. Liu, K. Yang, Y.D. Chen, X. Zhao, K. Wang, H. Lin, S. Lv, Peroxymonosulfate activation by oxygen vacancies-enriched MXene nano-$Co_3O_4$ co-catalyst for efficient degradation of refractory organic matter: Efficiency, mechanism, and stability, J. Hazard. Mater. 432 (2022), 128719, https://doi.org/10.1016/j.jhazmat.2022.128719.
[32] ATSDR, The ATSDR 2019 Substance Priority List, Division of Toxicology and Human Health Sciences Atlanta, GA (2019).
[33] W. Li, R. Xiao, J. Xu, H. Lin, K. Yang, W. Li, K. He, L. Tang, J. Chen, Y. Wu, S. Lv, Interface engineering strategy of a $Ti_4O_7$ ceramic membrane via graphene oxide nanoparticles toward efficient electrooxidation of 1,4-dioxane, Water Res. 216 (2022), 118287, https://doi.org/10.1016/j.watres.2022.118287.
[34] M. Sun, C. Lopez-Velandia, D.R. Knappe, Determination of 1,4-dioxane in the cape fear river watershed by heated purge-and-trap preconcentration and gas chromatography-mass spectrometry, Environ. Sci. Technol. 50 (2016) 2246–2254, https://doi.org/10.1021/acs.est.5b05875.
[35] C.S. Lee, A.K. Venkatesan, H.W. Walker, C.J. Gobler, Impact of groundwater quality and associated byproduct formation during UV/hydrogen peroxide treatment of 1,4-dioxane, Water Res. 173 (2020), 115534, https://doi.org/10.1016/j.watres.2020.115534.
[36] E.-T. Yun, S.-W. Park, H.J. Shin, H. Lee, D.-W. Kim, J. Lee, Peroxymonosulfate activation by carbon-encapsulated metal nanoparticles: Switching the primary reaction route and increasing chemical stability, Appl. Catal. B Environ. 279 (2020), 119360, https://doi.org/10.1016/j.apcatb.2020.119360.
[37] Z. Liu, H. Ding, C. Zhao, T. Wang, P. Wang, D.D. Dionysiou, Electrochemical activation of peroxymonosulfate with ACF cathode: Kinetics, influencing factors, mechanism, and application potential, Water Res. 159 (2019) 111–121, https://doi.org/10.1016/j.watres.2019.04.052.
[38] H. Wang, W. Guo, B. Liu, Q. Wu, H. Luo, Q. Zhao, Q. Si, F. Sseguya, N. Ren, Edge-nitrogenated biochar for efficient peroxydisulfate activation: An electron transfer mechanism, Water Res. 160 (2019) 405–414, https://doi.org/10.1016/j.watres.2019.05.059.
[39] J.A. Zazo, G. Pliego, P. García-Muñoz, J.A. Casas, J.J. Rodriguez, UV-LED assisted catalytic wet peroxide oxidation with a Fe(II)-Fe(III)/activated carbon catalyst, Appl. Catal. B Environ. 192 (2016) 350–356, https://doi.org/10.1016/j.apcatb.2016.04.010.
[40] S.J. Clark, M.D. Segall, C.J. Pickard, P.J. Hasnip, M.I.J. Probert, K. Refson, M. C. Payne, First principles methods using CASTEP, Z. Krist. Cryst. Mater. 220 (2005) 567–570, https://doi.org/10.1524/zkri.220.5.567.65075.
[41] C. Peng, X. Yang, Y. Li, H. Yu, H. Wang, F. Peng, Hybrids of two-dimensional $Ti_3C_2$ and $TiO_2$ exposing {001} facets toward enhanced photocatalytic activity, ACS Appl. Mater. Interfaces 8 (2016) 6051–6060, https://doi.org/10.1021/acsami.5b11973.
[42] J.P. Perdew, K. Burke, M. Ernzerhof, Generalized gradient approximation made simple, Phys. Rev. Lett. 77 (1996) 3865–3868, https://doi.org/10.1103/PhysRevLett.77.3865.
[43] F. Ortmann, F. Bechstedt, W.G. Schmidt, Semiempirical van der Waals correction to the density functional description of solids and molecular structures, Phys. Rev. B 73 (2006), https://doi.org/10.1103/PhysRevB.73.205101.
[44] B. Ahmed, D.H. Anjum, Y. Gogotsi, H.N. Alshareef, Atomic layer deposition of $SnO_2$ on MXene for Li-ion battery anodes, Nano Energy 34 (2017) 249–256, https://doi.org/10.1016/j.nanoen.2017.02.043.
[45] C. Sun, L. Wang, W. Zhao, L. Xie, J. Wang, J. Li, B. Li, S. Liu, Z. Zhuang, Q. Zhao, Atomic-level design of active site on two-dimensional $MoS_2$ toward efficient hydrogen evolution: experiment, theory, and artificial intelligence modelling, Adv. Funct. Mater. 32 (2022), https://doi.org/10.1002/adfm.202206163.
[46] Y. Gong, X. Zhao, H. Zhang, B. Yang, K. Xiao, T. Guo, J. Zhang, H. Shao, Y. Wang, G. Yu, MOF-derived nitrogen doped carbon modified g-$C_3N_4$ heterostructure composite with enhanced photocatalytic activity for bisphenol A degradation with peroxymonosulfate under visible light irradiation, Appl. Catal. B Environ. 233 (2018) 35–45, https://doi.org/10.1016/j.apcatb.2018.03.077.
[47] Y. Li, J. Ma, T.D. Waite, M.R. Hoffmann, Z. Wang, Development of a mechanically flexible 2D-MXene membrane cathode for selective electrochemical reduction of nitrate to $N_2$: mechanisms and implications, Environ. Sci. Technol. 55 (2021) 10695–10703, https://doi.org/10.1021/acs.est.1c00264.
[48] M. Ma, S. You, G. Liu, J. Qu, N. Ren, Macroporous monolithic Magnéli-phase titanium suboxides as anode material for effective bioelectricity generation in microbial fuel cells, J. Mater. Chem. A 4 (2016) 18002–18007, https://doi.org/10.1039/c6ta07521e.
[49] L. Deng, F. Hu, M. Ma, S.C. Huang, Y. Xiong, H.Y. Chen, L. Li, S. Peng, Electronic modulation caused by interfacial Ni-O-M (M=Ru, Ir, Pd) conding for accelerating hydrogen evolution kinetics, Angew. Chem. Int. Ed. Engl. 60 (2021) 22276–22282, https://doi.org/10.1002/anie.202110374.
[50] Z. Su, W. Yang, C. Wang, S. Xiong, X. Cao, Y. Peng, W. Si, Y. Weng, M. Xue, J. Li, Roles of oxygen vacancies in the bulk and surface of $CeO_2$ for toluene catalytic combustion, Environ. Sci. Technol. 54 (2020) 12684–12692, https://doi.org/10.1021/acs.est.0c03981.
[51] Q.V. Ly, L. Cui, M.B. Asif, W. Khan, L.D. Nghiem, Y. Hwang, Z. Zhang, Membrane-based nanoconfined heterogeneous catalysis for water purification: A critical review, Water Res. 230 (2023), 119577, https://doi.org/10.1016/j.watres.2023.119577.
[52] S. Zhang, M. Sun, T. Hedtke, A. Deshmukh, X. Zhou, S. Weon, M. Elimelech, J. H. Kim, Mechanism of heterogeneous Fenton reaction kinetics enhancement under nanoscale spatial confinement, Environ. Sci. Technol. 54 (2020) 10868–10875, https://doi.org/10.1021/acs.est.0c02192.
[53] S. Zhang, T. Hedtke, L. Wang, X. Wang, T. Cao, M. Elimelech, J.H. Kim, Engineered nanoconfinement accelerating spontaneous manganese-catalyzed degradation of organic contaminants, Environ. Sci. Technol. 55 (2021) 16708–16715, https://doi.org/10.1021/acs.est.1c06551.
[54] W. Chen, Y. Luo, G. Ran, Q. Li, An investigation of refractory organics in membrane bioreactor effluent following the treatment of landfill leachate by the $O_3/H_2O_2$ and MW/PS processes, Waste Manag. 97 (2019) 1–9, https://doi.org/10.1016/j.wasman.2019.07.016.
[55] J. Ye, Y. Wang, Z. Li, D. Yang, C. Li, Y. Yan, J. Dai, 2D confinement freestanding graphene oxide composite membranes with enriched oxygen vacancies for enhanced organic contaminants removal via peroxymonosulfate activation, J. Hazard. Mater. 417 (2021), 126028, https://doi.org/10.1016/j.jhazmat.2021.126028.
[56] J. Ye, J. Dai, C. Li, Y. Yan, Lawn-like $Co_3O_4$@N-doped carbon-based catalytic self-cleaning membrane with peroxymonosulfate activation: A highly efficient singlet oxygen dominated process for sulfamethoxazole degradation, Chem. Eng. J. 421 (2021), 127805, https://doi.org/10.1016/j.cej.2020.127805.
[57] S. Almassi, Z. Li, W. Xu, C. Pu, T. Zeng, B.P. Chaplin, Simultaneous adsorption and electrochemical reduction of N-nitrosodimethylamine using carbon-$Ti_4O_7$ composite reactive electrochemical membranes, Environ. Sci. Technol. 53 (2019) 928–937, https://doi.org/10.1021/acs.est.8b05933.
[58] L. Jin, S. You, N. Ren, B. Ding, Y. Liu, Mo vacancy-mediated activation of peroxymonosulfate for ultrafast micropollutant removal using an electrified MXene filter functionalized with Fe single atoms, Environ. Sci. Technol. 56 (2022) 11750–11759, https://doi.org/10.1021/acs.est.2c03904.
[59] Z. Yang, J. Qian, A. Yu, B. Pan, Singlet oxygen mediated iron-based Fenton-like catalysis under nanoconfinement, Proc. Natl. Acad. Sci. USA 116 (2019) 6659–6664, https://doi.org/10.1073/pnas.1819382116.
[60] Y. Zhou, J. Jiang, Y. Gao, S.Y. Pang, Y. Yang, J. Ma, J. Gu, J. Li, Z. Wang, L. H. Wang, L.P. Yuan, Y. Yang, Activation of peroxymonosulfate by phenols: Important role of quinone intermediates and involvement of singlet oxygen, Water Res. 125 (2017) 209–218, https://doi.org/10.1016/j.watres.2017.08.049.
[61] P. Sun, H. Liu, M. Feng, L. Guo, Z. Zhai, Y. Fang, X. Zhang, V.K. Sharma, Nitrogen-sulfur co-doped industrial graphene as an efficient peroxymonosulfate activator: Singlet oxygen-dominated catalytic degradation of organic contaminants, Appl. Catal. B Environ. 251 (2019) 335–345, https://doi.org/10.1016/j.apcatb.2019.03.085.
[62] E.T. Yun, J.H. Lee, J. Kim, H.D. Park, J. Lee, Identifying the nonradical mechanism in the peroxymonosulfate activation process: Singlet oxygenation versus mediated electron transfer, Environ. Sci. Technol. 52 (2018) 7032–7042, https://doi.org/10.1021/acs.est.8b00959.
[63] Y. Zong, X. Guan, J. Xu, Y. Feng, Y. Mao, L. Xu, H. Chu, D. Wu, Unraveling the overlooked involvement of high-valent cobalt-oxo species generated from the cobalt(II)-activated peroxymonosulfate process, Environ. Sci. Technol. 54 (2020) 16231–16239, https://doi.org/10.1021/acs.est.0c06808.
[64] W. Ren, C. Cheng, P. Shao, X. Luo, H. Zhang, S. Wang, X. Duan, Origins of electron-transfer regime in persulfate-based nonradical oxidation processes, Environ. Sci. Technol. 56 (2022) 78–97, https://doi.org/10.1021/acs.est.1c05374.
[65] J. Qi, X. Yang, P.Y. Pan, T. Huang, X. Yang, C.C. Wang, W. Liu, Interface engineering of $Co(OH)_2$ nanosheets growing on the $KNbO_3$ perovskite based on electronic structure modulation for enhanced peroxymonosulfate activation, Environ. Sci. Technol. 56 (2022) 5200–5212, https://doi.org/10.1021/acs.est.1c08806.
[66] C. Ren, X. Jia, W. Zhang, D. Hou, Z. Xia, D. Huang, J. Hu, S. Chen, S. Gao, Hierarchical porous integrated $Co_{1-x}S/CoFe_2O_4$@rGO nanoflowers fabricated via temperature-controlled in situ calcining sulfurization of multivariate CoFe-MOF-74@rGO for high-performance supercapacitor, Adv. Funct. Mater. 30 (2020) 2004519, https://doi.org/10.1002/adfm.202004519.
[67] J. Li, Z. Li, X. Liu, C. Li, Y. Zheng, K.W.K. Yeung, Z. Cui, Y. Liang, S. Zhu, W. Hu, Y. Qi, T. Zhang, X. Wang, S. Wu, Interfacial engineering of $Bi_2S_3/Ti_3C_2T_x$ MXene

based on work function for rapid photo-excited bacteria-killing, Nat. Commun. 12 (2021) 1224, 10.1038/s41467-021-21435-6.

[68] P. Xia, S. Cao, B. Zhu, M. Liu, M. Shi, J. Yu, Y. Zhang, Designing a 0D/2D S-scheme heterojunction over polymeric carbon nitride for visible-light photocatalytic inactivation of bacteria, Angew. Chem. Int. Ed. Engl. 59 (2020) 5218–5225, https://doi.org/10.1002/anie.201916012.

[69] Y. Wang, X. Li, M. Zhang, Y. Zhou, D. Rao, C. Zhong, J. Zhang, X. Han, W. Hu, Y. Zhang, K. Zaghib, Y. Wang, Y. Deng, Lattice-strain engineering of homogeneous $NiS_{0.5}$ $Se_{0.5}$ core-shell nanostructure as a highly efficient and robust electrocatalyst for overall water splitting, Adv. Mater. 32 (2020), e2000231, https://doi.org/10.1002/adma.202000231.

[70] S. Jiao, X. Fu, H. Huang, Descriptors for the evaluation of electrocatalytic reactions: d-band theory and beyond, Adv. Funct. Mater. 32 (2021) 2107651, https://doi.org/10.1002/adfm.202107651.

[71] S. Wang, L. Xu, J. Wang, Iron-based dual active site-mediated peroxymonosulfate activation for the degradation of emerging organic pollutants, Environ. Sci. Technol. 55 (2021) 15412–15422, https://doi.org/10.1021/acs.est.1c06205.

[72] J. Hu, Y. Li, Y. Zou, L. Lin, B. Li, X.-y Li, Transition metal single-atom embedded on N-doped carbon as a catalyst for peroxymonosulfate activation: A DFT study, Chem. Eng. J. 437 (2022), https://doi.org/10.1016/j.cej.2022.135428.

[73] W. Ni, A. Krammer, C.S. Hsu, H.M. Chen, A. Schüler, X. Hu, $Ni_3N$ as an active hydrogen oxidation reaction catalyst in alkaline medium, Angew. Chem. Int. Ed. 131 (2019) 7523–7527, https://doi.org/10.1002/ange.201902751.

[74] Y. Wen, J. Qi, D. Zhao, J. Liu, P. Wei, X. Kang, X. Li, O doping hierarchical NiCoP/$Ni_2P$ hybrid with modulated electron density for efficient alkaline hydrogen evolution reaction, Appl. Catal. B Environ. 293 (2021), 120196, https://doi.org/10.1016/j.apcatb.2021.120196.

[75] Z. Lv, W. Ma, M. Wang, J. Dang, K. Jian, D. Liu, D. Huang, Co-constructing interfaces of multiheterostructure on MXene ($Ti_3C_2T_x$)-modified 3D self-supporting electrode for ultraefficient electrocatalytic HER in alkaline media, Adv. Funct. Mater. 31 (2021), https://doi.org/10.1002/adfm.202102576.

[76] Y. Liu, Q. Lin, Y. Guo, J. Zhao, X. Luo, H. Zhang, G. Li, H. Liang, The nitrogen-doped multi-walled carbon nanotubes modified membrane activated peroxymonosulfate for enhanced degradation of organics and membrane fouling mitigation in natural waters treatment, Water Res. 209 (2021), 117960, https://doi.org/10.1016/j.watres.2021.117960.

[77] H. Wu, X. Xu, L. Shi, Y. Yin, L.C. Zhang, Z. Wu, X. Duan, S. Wang, H. Sun, Manganese oxide integrated catalytic ceramic membrane for degradation of organic pollutants using sulfate radicals, Water Res. 167 (2019), 115110, https://doi.org/10.1016/j.watres.2019.115110.

[78] M.B. Asif, H. Kang, Z. Zhang, Gravity-driven layered double hydroxide nanosheet membrane activated peroxymonosulfate system for micropollutant degradation, J. Hazard. Mater. 425 (2022), 127988, https://doi.org/10.1016/j.jhazmat.2021.127988.